Innovative Food Science and Emerging Technologies 73 (2021) 102763

Contents lists available at ScienceDirect

Innovative Food Science and Emerging Technologies

journal homepage: www.elsevier.com/locate/ifset

Small-angle neutron scattering reveals basis for composition dependence of gel behaviour in oleic acid - sodium oleate oleogels

Steven Cornet [a], Liliana de Campo [b], Marta Martínez-Sanz [b,1], Elke Scholten [a], Elliot Paul Gilbert [b,c,*]

[a] Physics and Physical Chemistry of Foods, Wageningen University, P.O. Box 17, 6700 AA Wageningen, the Netherlands
[b] Australian Centre for Neutron Scattering, Australian Nuclear Science and Technology Organisation, Locked Bag 2001, Kirrawee DC, NSW 2232, Australia
[c] Australian Institute for Bioengineering and Nanotechnology and Centre for Nutrition and Food Sciences, The University of Queensland, St. Lucia, Brisbane, QLD 4072, Australia

ARTICLE INFO

Keywords:
Oleogel
Lipid
Neutron scattering
Self-assembly
Oleic acid
Sodium oleate

ABSTRACT

The relationship between gel strength and structure on the micro- and nano-scale has been investigated for oleogels prepared in a range of triglyceride (TAG) oils (sunflower, olive, medium chain triglyceride) using mixtures of oleic acid (OA) and sodium oleate (SO) as gelling agents. Microscopy indicated a reduction in crystal size with increasing SO content. Gel strength increased with SO concentration but, for a constant SO concentration, decreased with the addition of OA. Small-angle neutron scattering (SANS) and ultra-SANS was measured from the gels formed in the TAG oils, as well as in hexadecane oil, the latter employing solvent contrast variation, to study the structures formed in more detail. In both the TAG oils and in hexadecane, SO formed lamellar crystalline structures whose low q scattering was consistent with mass fractal-like behaviour (for 0:1 and 1:8 compositions). Further OA addition (1:4–2:1) resulted in the simultaneous presence of inverse micellar structures. We hypothesise that the negative effect of OA on gel strength is due to the partial dissolution of SO by OA and the loss of gel-mediating SO-based lamellar crystals. The variation in OA:SO ratio is demonstrated to provide control over mechanical properties via large-scale structure formation while the tunability of such gel properties using this mechanism potentially provides an alternative route to the use of solid fats for structuring food.

1. Introduction

Organic fluids can be structured into soft-solid materials, known as organogels, through the use of organogelators. Organogelators entrap and stabilize liquid oil through the formation of a space-spanning network. This network can be formed by crystalline particles, polymers or self-assembled structures. Several organogelators and combinations thereof are known to self-assemble into 3D networks. Some examples are mixtures of fatty acids and fatty alcohols (Hughes, Marangoni, Wright, Rogers, & Rush, 2009), lecithin and sorbitan tristearate (M. a. Rogers et al., 2014), and phytosterol and γ-oryzanol (Bot et al., 2012). Organogels have numerous potential applications in pharmaceuticals (Bhatia, Singh, Raza, Wadhwa, & Katare, 2013), optoelectronics (Babu, Prasanthkumar, & Ajayaghosh, 2012), photovoltaics (Kubo et al., 2001), biosensors (Gao et al., 2018) and lubricants (Ru, Fang, Gu, Jiang, & Liu, 2020). Edible organic fluids, such as triglyceride oils, can be gelled to obtain edible organogels, also known as oleogels. Such oleogels offer a promising route towards creating food materials with the properties of solid fats but without the need for high concentrations of saturated- or trans fatty acids.

A class of molecules that show potential to structure edible oils is based on oleate-complexes which comprise an unsaturated fatty acid (oleic acid) and its associated sodium soap (sodium oleate). Previous research indicated that oleic acid cannot function alone as an oleogelator but, in combination with sodium oleate, a stable gel can be formed (Nikiforidis, Gilbert, & Scholten, 2015). While the hydrophilic headgroups of both molecules interact via hydrogen bonding, the mechanism by which the molecules are able to structure edible oils is currently not understood. Some researchers have tried to rationalise the efficacy of organogelators by analysing numerous gelator-solvent combinations and linking it to miscibility parameters, such as the Hansen Solubility Parameters (HSPs) (Gravelle, Davidovich-Pinhas, Zetzl, Barbut, &

* Corresponding author at: Australian Centre for Neutron Scattering, Australian Nuclear Science and Technology Organisation, Locked Bag 2001, Kirrawee DC, NSW 2232, Australia.
E-mail address: elliot.gilbert@ansto.gov.au (E.P. Gilbert).
[1] Current address: Institute of Food Science Research (CSIC-UAM), Nicolás Cabrera, 9, 28049, Madrid, Spain

https://doi.org/10.1016/j.ifset.2021.102763
Received 13 May 2021; Received in revised form 9 July 2021; Accepted 13 July 2021
Available online 16 July 2021

Marangoni, 2015; Raynal & Bouteiller, 2011; Rogers, 2018; Sawalha et al., 2020). This approach has been shown to be useful for single-molecule organogelators by providing a range of HSPs in which the gelator molecules neither dissolve nor fully precipitate within the solvent. Sawalha et al. used the HSPs to illustrate the gelation of sterol systems and concluded that this approach holds provided that the type of structure, in their case tubules, is conserved (Sawalha et al., 2020). Hence, for systems based on two (or more) different molecules, the phase behaviour of the gelators may be of greater importance.

Nikiforidis et al. studied the oleic acid – sodium oleate system in sunflower oil at an oleogelator concentration of 16 wt% (Nikiforidis et al., 2015). To gain information on the nanoscale, small-angle neutron scattering (SANS) studies of related samples in decane were measured. Their investigations revealed that either inverse micellar phases or lamellar crystals were formed, depending on the ratio between oleic acid and sodium oleate molar ratio. However, there remained unresolved questions including the effect of oil type on gel formation and how the structures formed on the micro- and nano-scale relate to the macroscopic behaviour of the gels.

In the present study, different edible (TAG) oils were explored (medium chain triglycerides, olive oil and sunflower oil) as well as additional concentrations, and ratios of oleic acid to sodium oleate. While there are a number of studies on oleogelators in the literature, there are few that attempt to directly relate the nano- and microscale structure development to the macroscopic gel strength. The benefits of employing ultra- and conventional small-angle scattering techniques have been recently reviewed (Gilbert, 2019); they have been applied to study a variety of oleogel systems prepared using phytosterols (Bot et al., 2012), natural waxes (Martins, Cerqueira, Fasolin, Cunha, & Vicente, 2016), lecithin (Nikiforidis & Scholten, 2014), mono- and diglycerides (Rosen-Kligvasser & Davidovich-Pinhas, 2021), and ethylcellulose (Davidovich-Pinhas, Barbut, & Marangoni, 2016). While all except Bot et al. exclusively employed X-rays, here, small-angle scattering with neutron contrast variation is employed. This provides access across the macro-micro-nanoscale regimes and extends previous structural studies by more than two orders of magnitude in dimension, as well as highlights the role of the individual components. It is shown that sodium oleate is primarily responsible for the gel strength in oleic acid – sodium oleate oleogels, and that oleic acid has a detrimental effect on gel strength that is likely to arise from its ability to partially solubilise sodium oleate.

2. Experimental

2.1. Materials

Refined sunflower oil (SFO; Reddy, Vandemoortle B.V., The Netherlands) and refined olive oil (OO; Bertolli, Grupo Deoleo, Spain) were purchased from commercial sources. Medium chain triglyceride oil (MCT) was purchased from Cremer Oleo Division (Cremer Oleo GmbH & Co. KG, Germany). The approximate fatty acid composition of SFO is 3.7% C16:0, 2.0% C18:0, 2.3% C20:0, 31.5% C18:1, and 59.5% C18:2 and of OO is 11.5% C16:0, 2.0% C18:0, 0.2 C20:0, 78.4% C18:1 and 7.0% C18:2 (Kostik, Memeti, & Bauer, 2012). MCT contains primarily C8 and C10 (caprylic and capric acid) in a 60/40 ratio according to the supplier's specifications. Anhydrous n-hexadecane $C_{16}H_{34}$ ($C_{16}H$) was purchased from Sigma-Aldrich (Steinheim, Germany). Deuterated n-hexadecane $C_{16}D_{34}$ with 99% deuteration ($C_{16}D$) was purchased from Cambridge Isotope Laboratories Inc. (Andover, MA, USA). Oleic acid (cis-9-octadecanoic acid; Fig. 1 right, a) $C_{18}H_{34}O_2$ (molecular weight 282.5 g/mol) and sodium oleate (cis-9-octadecenoic acid sodium salt; Fig. 1 right, b) $C_{18}H_{33}O_2Na$ (molecular weight 304.4 g/mol) were $\geq$ 99% pure and purchased from Sigma-Aldrich (Steinheim, Germany). Either milli-Q water (Millipore, Bedford, MA, USA) or deuterated water (D_2O) was used in all experiments. All materials were of reagent grade unless stated otherwise and were used as received. However, it is noted that the materials are of greater purity than those used in a prior study on similar systems (Nikiforidis et al., 2015). In the following, the abbreviations OA and SO will be used for oleic acid and sodium oleate, respectively.

2.2. Sample preparation

All samples were prepared on a weight-percent (wt%) basis by weighing water and oil with the subsequent addition of the structurants, OA and SO. Structurant mixtures were prepared in selected weight ratios of 2:1, 1:1, 1:2, 1:4, 1:8 and 0:1. For all oils, samples were prepared with a total structurant content of 16 wt%; additional samples were also prepared for SFO and hexadecane oils with total structurant content of 4 and 8 wt%. All samples contained 1 wt% water in total with the

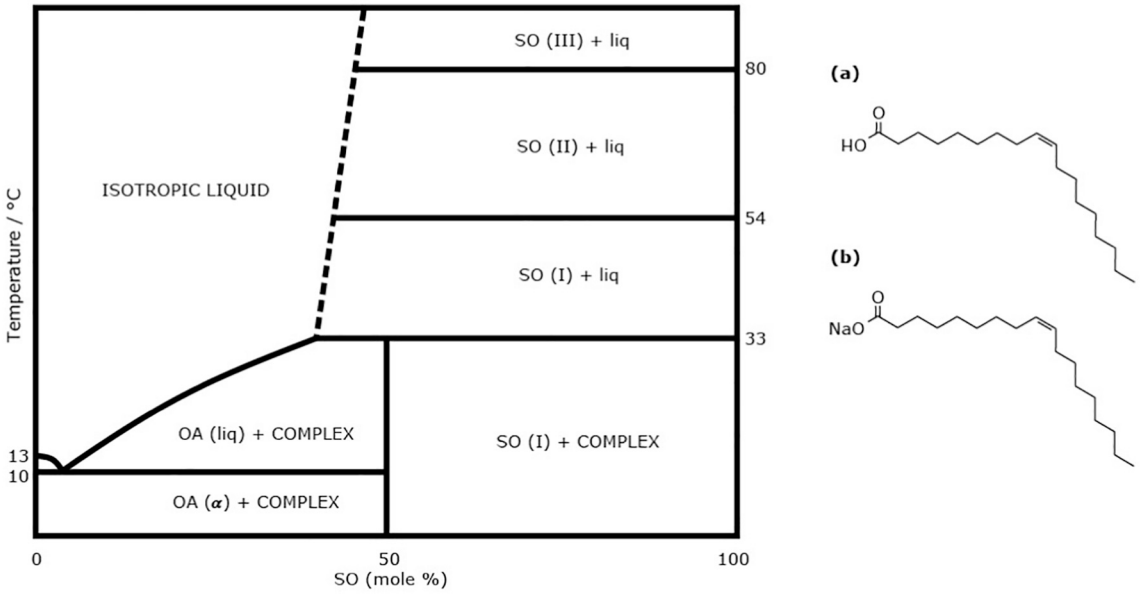

Fig. 1. (left) Phase diagram for OA:SO, adapted from (P. Tandon et al., 2001) with permission. Note that this diagram describes the phase behaviour in the absence of solvents. (right) Molecular structure of oleic acid (a) and sodium oleate (b).

remainder of the formulations being the respective oil. The structurant: water ratio thus depended on the structurant content. For a structurant ratio 0:1 prepared with $C_{16}H$, for example, this equates to a molar ratio of SO:H_2O:$C_{16}H$ of 1:1.06:6.97 for 16 wt%, 1:2.11:15.3 for 8 wt% and 1:4.23:31.9 for 4 wt%.

The sample preparation method was adapted from (Nikiforidis et al., 2015), with minor modification. In the original method, an Ultra-Turrax (IKA) was used to disperse the material, followed by stirring and heating at 80 °C. However, sample volumes of less than 5 mL could not be adequately mixed with the Ultra-Turrax and led to air being whipped into the sample. Samples were therefore mixed using a Branson Sonifier 250 ultrasonic probe (Branson Ultrasonics, Danbury, CT, USA) fitted with a micro-tip for approx. 1 min at a duty cycle setting of 10% on output level 7. This was enough to obtain a homogeneous mixture. The samples were subsequently placed in a floating Styrofoam tray in a preheated Julabo water bath (Julabo GmbH, Seelbach, Germany) at 80 °C for 20 min. Samples were allowed to cool at room temperature (20 °C) and aged at 5 °C for 96 h in a refrigerator, followed by 72 h at room temperature. For SANS experiments, selected samples were also prepared using deuterated materials (e.g. D_2O instead of H_2O and n-hexadecane-D_{34} instead of n-hexadecane-H_{34}) to enhance scattering contrast as discussed below. Sample composition is indicated by HD, DH, or DD, with the first and second letters indicating whether the oil phase (e.g. TAG oil or n-hexadecane) or 1% water component, respectively, is hydrogenated (H) or deuterated (D). As deuterated triglyceride oils are not readily available, only the HD contrasts were prepared for the edible gels.

2.3. Assessment of gel strength

Gel strength was determined using a stress-controlled Anton Paar rheometer (MCR 502, Anton Paar GmbH, Austria) with a parallel plate geometry with a diameter of 50 mm and gap of 1 mm. A Peltier element with a continuous flow of water maintained a constant temperature of 20 ± 0.1 °C. The sample was placed between the two plates and excess sample was removed. Samples were equilibrated for 5 min at 20 °C before measuring ($\gamma = 0$). Gel strength was determined at a frequency of $\omega = 0.172$ Hz and a strain amplitude, γ, of 0.01, which was in the linear viscoelastic regime. Gel strength is reported as the complex modulus, G^*, which provides a measure for the total energy stored and dissipated upon deformation. G^* is calculated as $G^* = \sqrt{G'2 + G''2}$ where G' and G" are the storage and loss moduli respectively. A qualitative assessment of gel strength was performed by spooning a sample from its container onto a flat surface. If the sample flowed or collapsed under its own weight it was considered a liquid; if a sample did not collapse it was considered a gel.

2.4. Polarised light microscopy

Microstructure of the aged samples was assessed using two polarising filters on a Zeiss Axioskop light microscope, fitted with a Zeiss Axiocam HRc camera (Carl Zeiss GmbH, Jena, Germany) to digitally record the micrographs. Zeiss Plan-Neofluar objectives (Carl Zeiss GmbH, Jena, Germany) with 10×/0.3 and 40×/0.65 magnification/objective lenses were employed. A small amount of the aged samples were placed on a glass slide and covered with a thin cover slip.

2.5. Small angle neutron scattering (SANS) and small angle X-ray scattering (SAXS)

Small Angle Neutron Scattering (SANS) experiments were performed on the QUOKKA SANS instrument (Gilbert, Schulz, & Noakes, 2006; Wood et al., 2018) located at the OPAL reactor at ANSTO, Australia. Three configurations were used to cover a q range of 0.004–0.7 $Å^{-1}$ where q is the magnitude of the scattering vector = $(4\pi/\lambda)\sin(\theta)$, λ is the wavelength and 2θ is the scattering angle. These configurations were: (i) source-to-sample distance (SSD) = sample-to-detector distance (SDD) = 20 m, (ii) SSD = SDD = 12 m and (iii) SSD = 12 m and SDD = 1.3 m with 500 mm detector offset, using a λ of 5 Å with 10% resolution, and source and sample aperture diameters of 50 mm and 12.5 mm respectively. All samples were loaded into demountable sample cells with path lengths of 1.0 mm. An automated 20 position sample changer was used operating at ambient temperature. Data were reduced using the NCNR SANS reduction macros (Kline, 2006) modified for QUOKKA, using the Igor software package (Wavemetrics, Lake Oswego, OR) with data corrected for solvent scattering, transmission and detector sensitivity. Data were transformed onto an absolute scale using attenuated direct beam transmission measurements. SANS data, by convention, are represented in reciprocal space and expressed as the scattering intensity versus q. q, with units of inverse Angstrom ($Å^{-1}$), relates the scattering to real space structure via an inverse relationship such that scattering at smaller angles reveals structure on larger length scales. More details on the application of small angle scattering methods to food materials can be found in (Gilbert, 2019). Data have been analysed using either macros written in the Igor software package or SASView (www.sasview.org).

SAXS measurements were performed on a Bruker Nanostar with a rotating anode source operated at a wavelength of 1.5418 Å (Cu K_α) with a sample-to detector distance of 730 mm, giving a q range from 0.0121 to 0.391 $Å^{-1}$. The optics and sample chamber were under vacuum to minimize air scattering. The samples were presented to the X-ray beam in sealed 2 mm sealed quartz capillaries (Hilgenburg Gmbh, Germany) and the scattering was measured for 60 min at room temperature. The scattering patterns were reduced and radially averaged with Bruker software. A scattering background from a quartz capillary filled with respective TAG oil was subtracted after correction for sample transmission.

The chemical formulae, physical densities and neutron scattering length densities for the components investigated are shown in Table 1.

2.6. Ultra-small angle neutron scattering (USANS)

Ultra-small angle neutron scattering (USANS) experiments were performed on selected samples on the KOOKABURRA instrument at the OPAL reactor (Rehm et al., 2018; Rehm, Brûlé, Freund, & Kennedy, 2013). All samples were loaded into demountable sample cells with path lengths of 0.17 mm and cross-section of 50 × 50 mm. Using a neutron wavelength of 4.74 Å and a sample aperture with a diameter of 35 mm, a q-range of ≈ 3×10^{-5}–0.007 $Å^{-1}$ was accessed. Rocking curve profiles were measured by rotating the analyser crystal away from the aligned peak position (the position at which the undeviated neutrons are

Table 1
Chemical formulae, physical densities and neutron scattering length densities (SLD) for the components in the study. SLDs were determined using https://sld-calculator.appspot.com. OO values based on triolein, SFO based on equimolar mixture of triolein and trilinolein ($C_{57}H_{104}O_6$) and MCT based on equimolar mixture of tricaprylin ($C_{27}H_{50}O_6$) and tricaprin ($C_{33}H_{62}O_6$).

	Chemical formula	Physical density (g/cm^3)	Neutron SLD (10^{-6} $Å^{-2}$)
Water (hydrogenated)	H_2O	1.00	−0.560
Water (deuterated)	D_2O	1.11	6.34
Hexadecane H_{34} ($C_{16}H$) (hydrogenated)	$C_{16}H_{34}$	0.770	−0.440
Hexadecane D_{34} ($C_{16}D$) (deuterated)	$C_{16}D_{34}$	0.887	6.74
Sunflower oil (SFO)	$C_{57}H_{101}O_6$	0.919	0.225
Olive oil (OO)	$C_{57}H_{104}O_6$	0.919	0.458
Medium chain triglyceride oil (MCT)	$C_{30}H_{56}O_6$	0.945	0.0275
Oleic acid (OA)	$C_{18}H_{34}O_2$	0.895	0.0784
Sodium oleate (SO)	$C_{18}H_{33}O_2Na$	0.90	0.204

reflected onto the detector) and measuring the neutron intensity as a function of q. The USANS data were reduced with an empty cell as background and converted onto an absolute scale using adapted python scripts based on NCNR USANS reduction macros (Kline, 2006). The reduced slit-smeared data were desmeared using the Lake algorithm (Kline, 2006) before merging with the QUOKKA data. Note that the combination of access to lower q SANS configurations on QUOKKA, as well as USANS, extend the minimum q and therefore size range by a factor of more than two orders of magnitude compared to previous studies (Nikiforidis et al., 2015) enabling substantial new insights into these gel systems.

3. Results and discussion

3.1. Visual observations

During preparation and subsequent ageing of the gels, changes in appearance were observed depending on the structurant composition. An overview of the gel appearance is presented in Table 2. Samples prepared with oleic acid:sodium oleate (OA:SO) ratios of 2:1 and 1:1, regardless of the triglyceride (TAG) oil used, formed transparent liquids upon heating. This suggests sufficient dissolution of all components on a length scale below that of visible light (≈ 400 nm). Upon cooling and ageing, these samples became opaque indicating re-crystallization or precipitation of the dissolved structurant. Most of the 2:1 samples, which contained primarily OA, remained viscous liquids after ageing. All 1:1 samples, except at 4 wt% structurant, became spreadable soft-solid materials after ageing. Samples containing larger fractions of SO (ratios 1:2, 1:4, 1:8, 0:1) became opaque and viscous materials upon heating. Cooling and subsequent ageing of these samples induced gelation and yielded opaque, spreadable and self-supporting gels that remained stable for several months.

The transparency observed for samples with low SO content and opacity for higher SO contents shows an apparent dependence on the OA:SO ratio. The phase diagram of OA and SO reported by Tandon et al. (2001), adapted in Fig. 1, may provide an insight for this dependence (Tandon, Raudenkolb, Neubert, Rettig, & Wartewig, 2001a). The addition of OA to SO can lower the melting temperature of SO from 232 °C (pure SO) to <80 °C (the upper temperature used in the preparation of the gels). This is the likely explanation as to why the samples with greater OA became transparent upon heating, while samples with an excess of SO remained opaque. Of course, the phase diagram does not consider the influence of water nor oil; however, complementary DSC data from selected sample compositions have previously been reported in Nikiforidis et al. (Nikiforidis et al., 2015). Apart from the lack of gel formation of the 16 wt% 2:1 SFO and OO samples, the effect of the TAG oil on the visual appearance of the aged samples was limited to the differences in colour of the respective oil used, i.e. yellow, green and colourless for SFO, OO and MCT respectively.

Table 2
Observations of the extent of gel formation for TAG oil gels prepared with 4 wt%, 8 wt% and 16 wt% structurant as a percentage of the total gel weight. All samples contained 1 wt% water. OA:SO ratios correspond to the weight ratio of oleic acid to sodium oleate within the structurant used. *Showed signs of syneresis or yielding/'melting' upon handling.

	SFO			OO	MCT
	4 wt%	8 wt%	16 wt%	16 wt%	16 wt%
OA: SO					
2: 1	Liquid	Liquid	Liquid	Liquid	Gel*
1: 1	Liquid	Gel	Gel	Gel	Gel
1: 2	Liquid	Gel	Gel	Gel	Gel
1: 4	–	–	Gel	–	–
1: 8	–	–	Gel	–	–
0: 1	Gel	Gel	Gel	Gel	Gel

3.2. Microstructure

The influence of structurant composition and oil phase was assessed using polarised light microscopy as shown in Fig. 2 for SFO, and supplementary Fig. S 1 and Fig. S 2 for MCT and OO respectively. More complex structures were observed than previously reported by Nikiforidis et al. (2015); this may be related to the greater purity of components used here or differences in sample preparation and ageing. Samples prepared with SFO and 16 wt% structurant for 2:1 and 1:1 (Fig. 2) showed the presence of large crystalline structures with distinct shapes that exhibited birefringence under polarised light, which arise from their possessing crystallographically distinct axes. SFO samples with a 2:1 ratio contained a combination of ≈ 100 μm platelets, parallelepipeds and larger ≈ 200 μm structures. 1:1 contained what appear to be loosely packed structures, reminiscent of bowties, comprising needles of ≈ 500 by ≈ 7 μm dimension. SFO 1:2, 1:4 and 1:8, which contain increasing fractions of SO, showed aggregated, space filling networks of more numerous but smaller crystals with long dimensions of $\lessapprox$ 20 μm. For 0:1, a space-filling network of elongated crystals was observed. With increasing SO, there was a general trend to more numerous but smaller crystals.

The microstructures of MCT and OO gels (Supplementary Fig. S 1 and Fig. S 2 respectively) were similar to those for SFO, although some differences were observed for the OA-rich samples. Structurant ratio 2:1 with MCT showed bowtie structures larger than those observed for 1:1 SFO. With long dimensions up to ≈ 800 μm, the structures were large enough to be observed with the naked eye. For 1:1 MCT, the structures were smaller than for 1:1 SFO, and inhomogeneously distributed crystalline structures with different shapes were present. For 2:1 OO, parallelepipeds were observed similar to SFO 2:1, although their size (≈ 10 μm) was smaller than those in SFO. Additionally, spherical particles were observed for 2:1 OO. For 1:1 OO, an aggregated space-spanning network of needle-shaped structures was observed without the presence of bow-tie shaped structures. For both MCT and OO, the 1:2 and 0:1 samples showed an aggregated network of crystals.

Despite the differences in microstructure, there was a general trend of more numerous but smaller crystals with increasing SO content in all three oils. The phase diagram presented in Fig. 1 offers some explanation about the origin of the apparent relation between SO content and the number and size of crystals. According to the phase diagram, an isotropic liquid phase forms at temperatures greater than 33 °C until the OA content falls below the equimolar ratio. This, as discussed in Section 3.1, can explain the observed transparency at 80 °C with OA effectively solubilizing SO. For increasing SO content, less SO is able to dissolve upon heating to 80 °C. Hence, some SO inevitably remains crystalline throughout the sample preparation process, resulting in the observed opacity. These SO crystals may act as nucleation sites for dissolved SO that can recrystallise during subsequent cooling and ageing. The presence of numerous nucleation sites would explain the large number of smaller crystals in the samples with a high SO content. For the samples in which all SO dissolved (2:1, 1:1) at 80 °C, a larger degree of quenching would be required to induce nucleation, and therefore the critical radius for crystal growth would be larger. The presence of fewer nucleation sites has the effect of forming fewer but larger crystals, as is indeed observed for the 2:1 and 1:1 samples in all oil types. Sawalha et al. showed subtle changes in solvent properties can have major effects on the properties of sterol-based organogels (Sawalha et al., 2020). The effect of solvent properties will be most notable in the regime where OA is the main contributor to the structurant by acting as a solubilizer for SO. The microscopy demonstrates that both the solvent and the structurant composition play a role in the appearance and, possibly, the type of crystals formed. As per the phase diagram in Fig. 1, OA and SO can form a co-crystal with an equimolar composition, which might be present for the samples containing both OA and SO. However, based on microscopy alone, the crystal type cannot be determined.

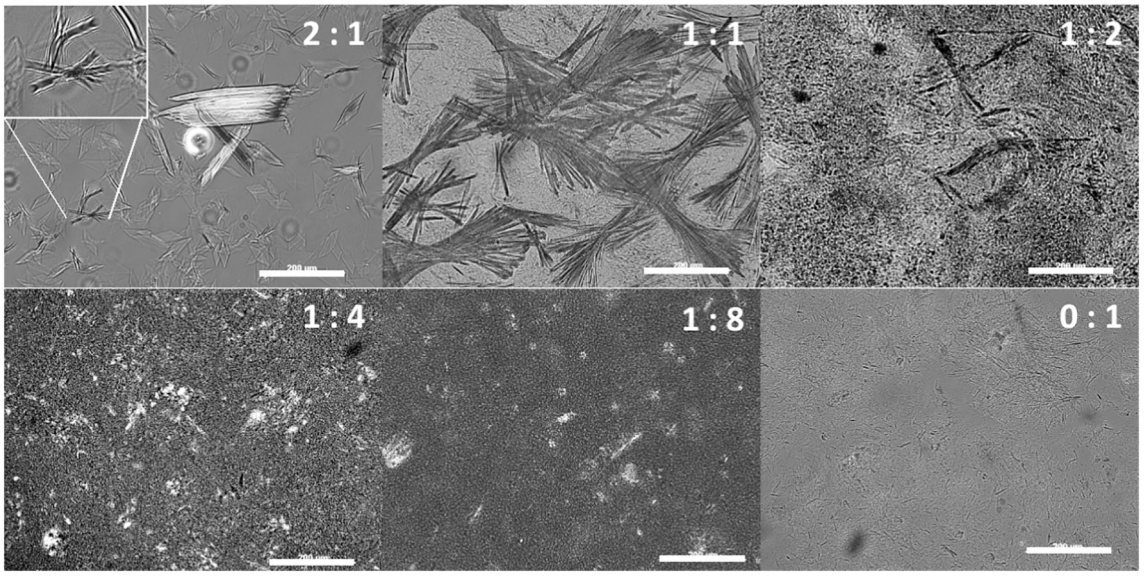

Fig. 2. Micrographs of oleogels prepared with sunflower oil with a total structurant concentration of 16 wt% and 1 wt% water (H_2O) as obtained using cross-polarizers. The oleic acid (OA) and sodium oleate (SO) ratio is shown for each micrograph. Scale bars are 200 μm.

3.3. Assessment of gel strength

The gel strength was determined with small amplitude oscillatory shear measurements. The loss tangent, tan **δ**, was of the order of unity for most samples, highlighting the visco-elastic nature of these oleogels (data not shown). While this would formally disqualify them as solids, these systems were self-supporting which makes their categorisation as solids, rather than liquids, reasonable. Indeed, all combinations of structurant and oil that formed gels (Table 2), including those with high values for tan **δ**, could be spread as a thick paste similar to e.g. shortening. The complex moduli, G*, of oleogels prepared with the different TAG oils are presented in Fig. 3 (a) for gels prepared using a structurant level of 16 wt% of the total sample mass. Of this 16 wt% structurant, the ratio of OA:SO was internally varied from 2:1 (i.e. 5.3 wt% SO and 10.7 wt% OA) to 0:1 (16 wt% SO). The gels containing solely SO as structurant (ratio 0:1) had the highest modulus for all three TAG oils. Gels containing primarily OA were considerably weaker, with the 2:1 16 wt% gels having the appearance of slurries. For the 2:1 samples, measured torque values approached the lower limit of the instrument, causing larger error bars. It was noted that a similar result was obtained when plotting the storage modulus, G', instead of G*, as a function of SO content. Frequency sweeps revealed that the modulus of most gels depends on the frequency via a power-law with an exponent between approx. 0.06 and 0.4 (data not shown). However, no relation between the power-law exponents and oleogel composition was found.

Based on Fig. 3 (a), G* appears to increase with SO content for all three TAG oils studied. These observations differ from an earlier study in which an OA:SO ratio of 1:1 resulted in the highest storage modulus (Nikiforidis et al., 2015). This discrepancy might relate to differences in preparation and component purity, as addressed in Section 2.1. It is noted that for SFO, for which additional OA:SO ratios were studied, there is an apparent plateau between the ratios 1:2 and 1:8. Based on Fig. 1, all structurant (both OA and SO) would be in a crystalline form at 25 °C via the formation of a co-crystal complex. If the modulus solely depended on the concentration of crystalline material and not on the specific structure of the crystalline material, this offers an explanation for the apparent plateau and the decrease in modulus for higher OA contents (< 4:6 OA:SO) where some OA is dissolved in the solvent thereby reducing complex formation. However, this does not explain the increase in elastic modulus when pure SO is used (ratio 0:1). This suggests that not only the solid content but also the structural organisation determines the rheological properties, which could explain the small differences in G^* between the different oils. Further details on the crystal structure is obtained using SANS and discussed subsequently.

Additional experiments were performed on SFO oleogels with total structurant concentrations of 4, 8, and 16 wt% (Fig. 3 b). The same general trend was observed, with the complex modulus increasing as a function of SO content. Interestingly, when comparing gels with different OA concentrations for the same SO content, large differences in G^* become apparent. For example, for a fixed SO concentration of 8 wt% SO, the 0:1 8 wt% gel had a greater modulus than the 1:1 16 wt% gel. Similarly, for a fixed SO concentration of 4 wt% SO, the 0:1 4 wt% gel had a greater modulus than the 1:1 8 wt% gel. The presence of OA thus appears to reduce the gel strength. While the origin of this detrimental effect is likely to be the solubilizing influence of OA on SO (Fig. 1), this cannot be confirmed based on the gel strength alone. Furthermore, the phase diagram considers only mixtures of OA and SO, while these oleogels contain both TAG oil and 1 wt% water.

Microscopy revealed a relationship between structurant composition and the presence and spatial distribution of micron-sized crystalline material. Rheology indicated that SO enhances the gel strength but also indicated a role for OA. To further study the effect of OA and SO on the resultant gel structures at the micron and sub-micron scale, additional experiments were performed using neutron scattering.

3.4. SANS of triglyceride-based oleogels

SANS patterns for the 1:1 and 0:1 16 wt% oleogels prepared with SFO, MCT, and OO are shown in Fig. 4. All patterns exhibit pseudo power-law scattering at low q and multiple Bragg diffraction peaks at higher q occurring at positions, q, 2q, 3q and 4q, indicative of a regular lamellar repeat. While the power-law scattering at low q is reminiscent of surface fractal-like structures (with exponent between ≈ −3 and −3.5), there is notable curvature with decreasing q indicating that this interpretation is far too simplistic, particularly for the samples based on SFO. The lack of a Guinier region indicates that the structural entities giving rise to this scattering have a size, L, greater than the inverse of the minimum q measured i.e. $L > \pi / q_{min}$ (≈ 1000 Å); they are denoted here as 'large-scale structure' to distinguish them from scattering features arising from the 'smaller' length scale, Bragg diffraction peaks. In comparing the 0:1 samples, the presence of curvature in the SFO scattering at low q and its absence in the OO and MCT samples implies that

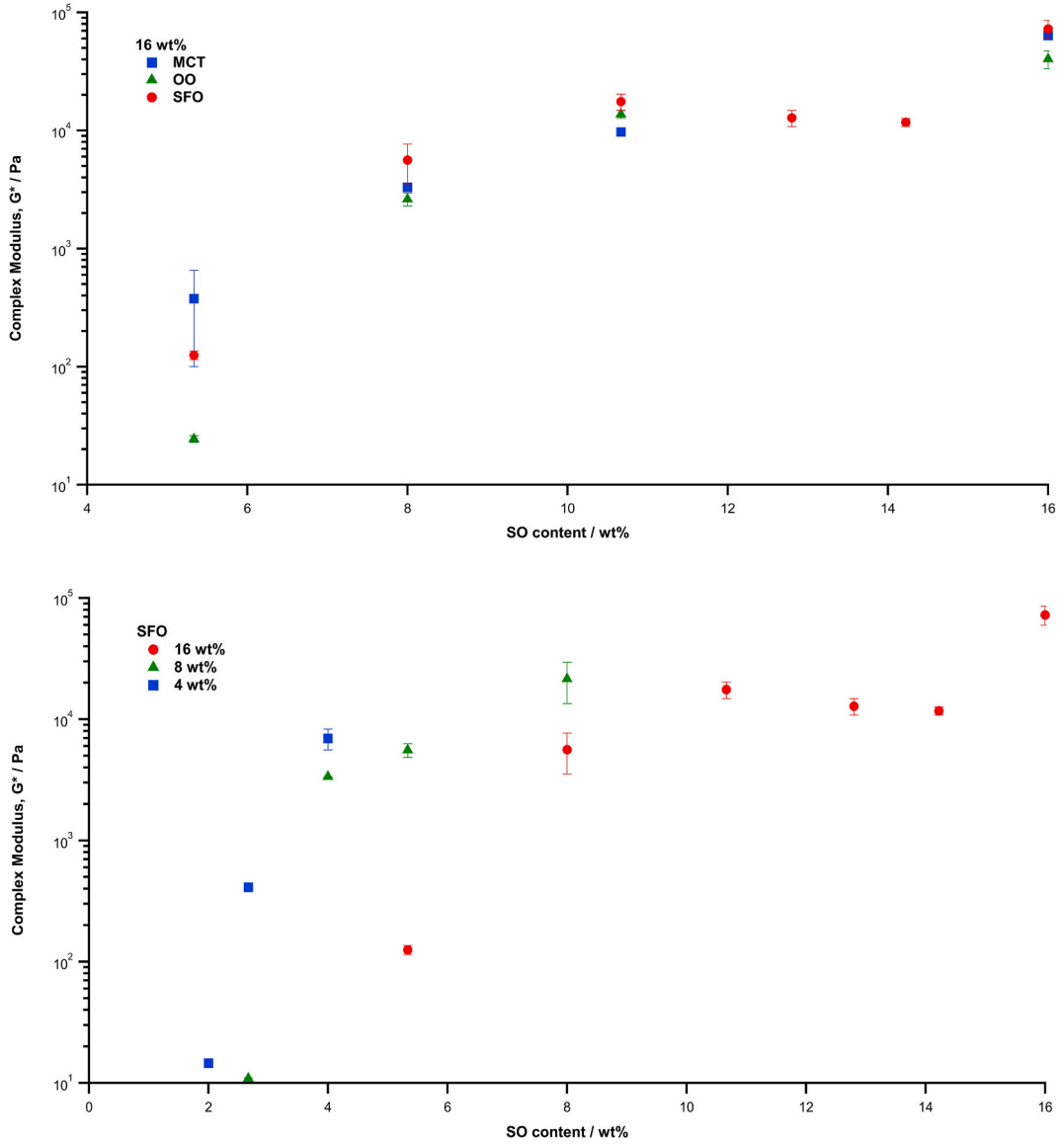

Fig. 3. (a) Complex moduli, G*, for oleogels prepared with 1 wt% water and a total structurant content of 16 wt% in sunflower oil (SFO), medium chain triglyceride oil (MCT) or olive oil (OO). (b) Complex moduli, G*, for oleogels prepared with 1 wt% water using sunflower oil (SFO) and a total structurant content of 4, 8 or 16 wt %. Moduli are reported as a function of sodium oleate (SO) content; the remainder of the structurant was oleic acid (OA). $n = 2$ with error bars indicating the absolute deviation from the mean.

the average size of the structures giving rise to the low q scattering are smaller for SFO. This is consistent with microscopy images although it is noted that the microscopy provides structural information on a much larger length scale.

For all 0:1 compositions, Bragg peaks are located at q ≈ 0.138 $Å^{-1}$, which corresponds to a d-spacing of 45.5 Å, as given by $d = 2\pi/q_{peak}$. This value is in reasonable agreement with the d-spacing for pure SO of 45.1 Å (Tandon, Neubert, & Wartewig, 2000). For the 1:1 samples, the peaks occur at a higher q of ≈ 0.140 $Å^{-1}$ (d ≈ 44.9 Å) i.e. OA addition leads to crystals with an overall shorter d-spacing. The reported d-spacing for the OA/SO complex is greater than SO at 46.1 Å (Tandon, Raudenkolb, Neubert, Rettig, & Wartewig, 2001a) while OA is smaller at 41.4 Å (Tandon, Förster, Neubert, & Wartewig, 2000). It is therefore likely that OA addition here results in the formation of mixed crystals rather than the complex, as discussed below. However, one must be cautious with such a conclusion as (i) indications of at least two crystal motifs were observed in the microscopy and thus two (or more) coexisting crystal structures may be contributing to the SANS and (ii) a variety of other crystal structures (for example, an increased internal angle can lead to shorter d-spacing), have been reported for OA and SO (Curat & Perron, 1977; Jandacek & Broering, 1989; Kaneko, Yamazaki, Kitagawa, & Kikyo, 1997; Tandon, Neubert, & Wartewig, 2000; Tandon, Raudenkolb, Neubert, Rettig, & Wartewig, 2001b; Unger, Chaturvedi, Mishra, Tandon, & Siesler, 2013). Fits to the SANS data using a power-law plus Gaussian peak model up to 0.2 $Å^{-1}$ (i.e. the region including the first Bragg peak) are summarised in Table 3. Due to the limited q range, the power law exponent merely acts as a fitting parameter and no major conclusions should be drawn. However, as far as the Bragg peaks are concerned, the effect of OA addition (cf. 0:1 with 1:1) consistently decreased their intensities as well as decreased the intensity of the power law scattering, indicating that these two scattering features are related.

The intensity in the limit of low q can be considered to be a measure of the total amount of large-scale structure in the system; a visual inspection of the SANS data as well as the scale factor for the power law function demonstrate that the low q scattering is significantly and consistently greater for the 0:1 compared to the 1:1 formulations. Preliminary SANS data for 2:1 and selected intermediate compositions confirm a general decrease in intensity with OA (data not shown). SANS

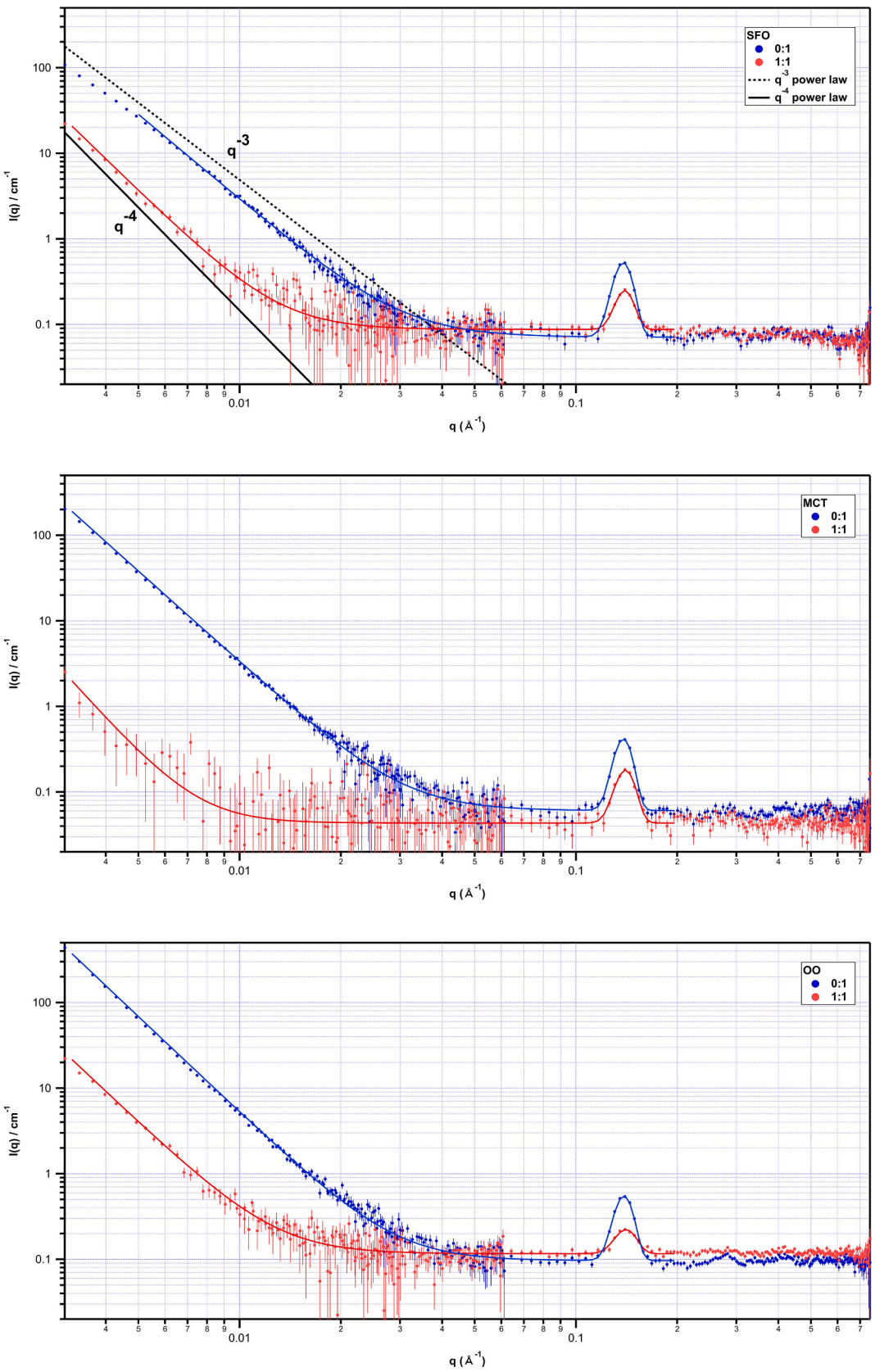

Fig. 4. SANS from 1:1 and 0:1 oleogels: (a) SFO (with q^{-4} and q^{-3} power law scattering superimposed); (b) MCT and (c) OO. Gels have been prepared with TAG oils (hydrogenated) and D_2O (deuterated) and are thus denoted as HD contrast. Fits using power-law plus Gaussian peak model shown as solid lines.

Table 3
Fits to SANS from 1:1 and 0:1 oleogels. SANS data are presented in Fig. 4. *Curvature apparent at low q. The standard deviation in the last digit of the fitting parameter is shown in parentheses.

	SFO		MCT		OO	
OA:SO	1:1	0:1*	1:1	0:1	1:1	0:1
Prefactor	1.0(2) x10^{-7}	1.05(7) x10^{-6}	1(3) x10^{-9}	1.21(4) x10^{-6}	1.7(3) x10^{-7}	7.5(2) x10^{-7}
Exponent	3.22(3)	3.20(1)	3.5(3)	3.197 (7)	3.14(3)	3.397 (5)
Bragg Intensity / cm^{-1}	0.33(5)	0.93(5)	0.25(3)	0.81(7)	0.16(2)	0.94(5)
Bragg q / $Å^{-1}$	0.1396 (3)	0.1381 (1)	0.1401 (4)	0.1382 (1)	0.1408 (5)	0.1388 (1)
Width Δq / $Å^{-1}$	0.0041 (7)	0.0040 (3)	0.0047 (7)	0.0036 (3)	0.0068 (8)	0.0040 (2)
d / Å	45.0	45.5	44.8	45.4	44.6	45.3

measurements of the oleogels, in concert with the microscopy, are revealing in terms of the presence and type of lamellar crystalline material present and the extent to which it may impact on the gel mechanical properties on larger length scales. While the SANS data are also reduced to an absolute scale, enabling a direct comparison between the datasets, they are nonetheless noisy. This is intrinsically due to the lack of scattering contrast within the samples. The solvents and structurants have similar values for the neutron scattering length density (Table 1) with deuterated water (D_2O) providing the principal contrasting agent within the samples. To fully exploit the capabilities of SANS, deuterated solvents and/or structurants should be used. The majority component in the gels is oil (comprising 83–95 wt% of the total) and thus the use of a deuterated oil is an obvious strategy. Since deuterated TAG oils are not readily available, a deuterated solvent analogue was used instead, namely the C_{16}-alkane hexadecane ($C_{16}H_{34}$), which can be readily acquired in deuterated form, $C_{16}D_{34}$. Of course, alkanes are purely apolar solvents unlike TAG oils; thus, although the substitution is not ideal, the additional insights obtained through the use of hexadecane proves to be invaluable in better understanding the TAG-based oleogels and particularly the influence of the OA:SO ratio.

3.5. SANS of C_{16}-based organogels

In the following, unless stated to the contrary, non-deuterated C_{16} and D_2O were used to prepare gels (HD contrast). Selected samples were also prepared using deuterated C_{16} alkane in combination with either H_2O or D_2O (DH and DD contrasts). For the C_{16}-based organogels, the SANS intensity in the limit of low q as a function of wt% of structurant is presented in Fig. 5 (a) for 4, 8, and 16 wt% organogels. It can be seen that, for a fixed OA:SO ratio, there is a linear relationship between intensity and the wt% of structurant in the gel i.e. the greater the structurant, the greater large scale structure.

The scattering intensity in the limit of low q was typically one order of magnitude greater for the organogels than for TAG-based oleogels. One could conclude that this arises from the lower polarity of the C_{16} solvent compared to the TAG oils resulting in a reduction in the solubility of the SO molecules and a greater degree of precipitation (i.e. more crystalline material and greater scattering intensity); however, such an assumption is unnecessary. For a simple two-phase system of crystalline structurant surrounded by oil, the low q intensity is proportional to the square of the scattering length density difference, or contrast, between the two components (Table 1):

$$I(q) = \frac{2\pi\varphi(1-\varphi)(\Delta\rho)^2}{q^4}\frac{S}{V}$$

where φ is the volume fraction of the 'large-scale network structure', Δρ is the contrast in neutron scattering length density (SLD) with respect to the oil and S/V is the interfacial surface area per unit volume. The

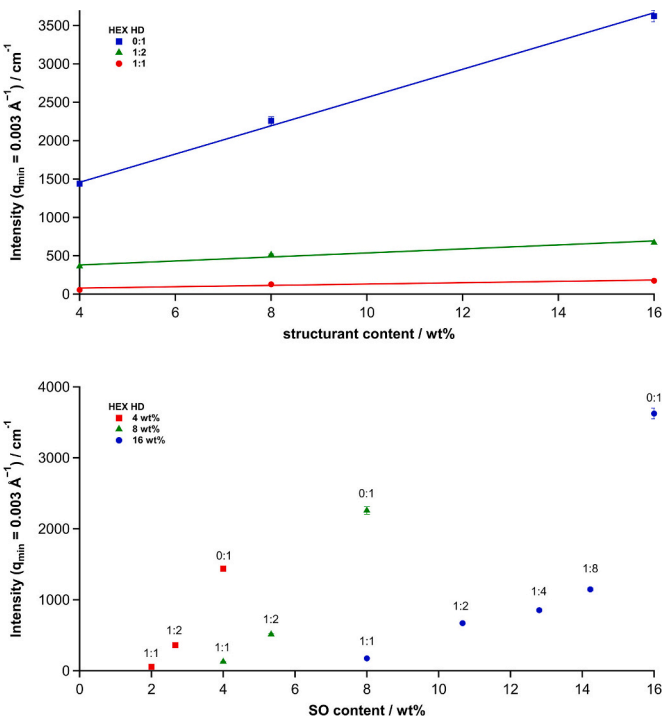

Fig. 5. SANS intensity at q_{min} = 0.003 $Å^{-1}$ for hexadecane-based organogels with HD contrast for 4, 8 and 16 wt% systems (a) as a function of the weight% structurant; and (b) as a function of the weight% SO; labels indicate associated OA:SO ratios.

greater intensity in the organogels can, in fact, be directly attributed to the greater neutron scattering length density difference between the structurant and hexadecane oil, as compared to the TAG oils.

It is far more illuminating to explore the influence of structurant composition. Fig. 5 (b) shows the variation in SANS intensity in the limit of low q as a function of SO wt% where OA:SO ratios are indicated in the labels. As observed in the TAG systems, there is a trend of increasing low q intensity with increasing SO content. However, the presence of OA has a clear negative effect as samples with the same amount of SO exhibit reduced intensity. This strongly suggests that the large-scale structures giving rise to this low q scattering are related to the observed composition-driven variations in gel strength.

From the equation above, the low q scattering for a two-phase system is also proportional to the interfacial area per unit volume. The fact that the variation in intensity increases dramatically and non-linearly with SO indicates that the crystalline material undergoing precipitation must also be more dispersed. Such behaviour is consistent with microscopy of the TAG oleogels where the presence of 'bow-tie' features was replaced by finer crystalline features at greater SO contents. The latter may indicate replacement of the one type of crystal structure with an SO-rich precipitate. Further structural information can be extracted from the small-angle scattering extended to even lower q using USANS.

3.6. Origin of the scattering

Before proceeding further, it is worthwhile at this stage reviewing the contrasts used and the extent to which different structural aspects of the gels are thereby highlighted. The structurant in all cases is hydrogenated. The HD contrast therefore identifies the location of deuterated water with respect to all other components in the system. The DH contrast highlights all the components with respect to the deuterated oil solvent and the DD contrast highlights the non-deuterated structurant with respect to all other components. As a consequence of this labelling strategy, one might expect that the large scale crystalline structures

giving rise to the low q scattering would be most apparent in the DD contrast, comparably so in the DH contrast but much less so in HD. In a similar way, different regions of inverse micelles are highlighted in HD (where only the core is observable), as a shell in DD and the entire micelle in DH. As far as Bragg peaks are concerned, i.e. on the size range of individual packed molecules, one might expect HD and DD to have similar intensities (i.e. independent of the oil contrast), and DH (and, indeed HH, if such a measurement were performed) to have smaller intensities, particularly if water is associated with charged headgroups in the structurant.

The C_{16} organogel SANS patterns are presented in Fig. 6 (Hex HD) and Fig. 7 (Hex DD) and show more features than observed in the TAG oleogel scattering (Fig. 4). This can be attributed to the greater scattering contrast between the hexadecane solvent, particularly when deuterated, and structurant; the latter highlights the value of SANS in combination with selective deuteration. As observed for the TAG samples, the HD samples exhibit increasing low q scattering with increasing SO composition with the Bragg peaks becoming increasingly resolved and intense at higher q. Only the 2:1 sample fails to exhibit an upturn in low q intensity, consistent with the formation of inverse micelles. The 0:1 sample exhibits a feature at $q \approx 0.055$ Å^{-1} which is discussed below.

The samples with the greatest contrast (C_{16} DD) with respect to the structurant were additionally studied with USANS. The combination of SANS and USANS provided information on length scales between approximately 20 μm and 1 nm. The scattering data thus overlaps, at the upper end, with the length scales accessed in the micrographs and, at the lower end, extend down to the length scale of a structurant molecule.

Combined USANS and SANS data for 16 wt% C_{16} with DD contrast are shown in Fig. 7. In this series, the SANS is dominated by the deuterated solvent and water contrasted against the hydrogenated structurant components. 2:1 exhibited inverse micellar scattering with no evidence of Bragg peaks. Still, some degree of large-scale structure formation was apparent at low q albeit whose intensity was approximately two orders of magnitude lower than that of the other compositions. Comparing 2:1, 1:1 and 1:2, the low-q intensity increased with SO content but the inverse micelle scattering persists. There is also evidence of the coexistence of Bragg peaks, and therefore crystalline material, at these compositions (Fig. S3) although they are somewhat swamped by the micelle scattering. At an OA:SO ratio of 1:4 the micellar feature moves to lower q indicating larger particles, which is accompanied by the emergence of multiple Bragg reflections, the first at $q \approx 0.15$ Å^{-1}. With this increasing amount of SO, such behaviour may be understood as a greater proportion of structurant forming a separate crystalline phase leaving less structurant available to form inverse micelles. As a consequence, the same number of water molecules must be stabilised by fewer structurant molecules, resulting in a larger inverse micelle core.

The micelle scattering is absent for 1:8 and 0:1 and the patterns are almost identical except that the Bragg peaks shift to lower q in 1:8 to 0:1 from 0.151 to 0.139 A^{-1}, indicating a larger d-spacing with increasing SO content, as was also observed for the TAG systems. Since the reported d-spacing for the OA/SO complex is greater than that of SO, the shift in spacing to greater distance with SO is therefore likely to be associated with a crystallographically impure SO lamellar crystal containing OA, and not a decreasing quantity of the complex.

The USANS region reveals details on larger length scales. A fit over the full q range for 0:1 covering approximately 10 orders of magnitude in intensity and 5 orders of magnitude in q is shown in Fig. 7b. The fit is based on a Guinier-Porod model combined with 5 Gaussian peaks (4 orders of reflections from a set of crystalline lamellar peaks at $q \approx 0.14$ Å^{-1} and the lower q peak at ≈ 0.055 Å^{-1}, as discussed below) with values of $R_g = 121$ Å, dimension variable of 2.42 and Porod exponent of 3.67. The dimension variable for a plate-like scatterer would be 2 and the associated R_g for such an object would enable the thickness, T, to be determined based on the relationship $T = \sqrt{(12)}R_g$. It is not inconceivable that the observed low q power slope could be associated with plate-like scattering particles, typical of lamellar crystals with exponent $= 2$ that itself is contaminated by the coexistence of higher exponent power laws associated with the Porod region of larger particles. Despite the acceptable Guinier-Porod model fit to the data, in the current case, the assembly of partially rough (Porod exponent < 4) crystalline particles undergoing mass fractal aggregation on a larger length scale is more structurally realistic and closer to microscopy observations. The USANS can therefore be equally well described with a double power law function, which yields a low q power-law slope of ≈ 2.4, indicating mass fractal-like behaviour, followed by a surface-fractal like slope of ≈ 3.8 (Table 4). The cross-over between these two regions occurs at a $q \approx 0.0029$ Å^{-1} and can be broadly associated with a dimension of $\approx \pi/q_{crossover} \approx 1080$ Å which is equivalent to approximately 24 longitudinal unit cell repeats of the structurant(s). This value is somewhat larger than observed in decane-based systems (Nikiforidis et al., 2015) where a crossover to Porod law scattering occurred at higher q. The average grain size, L, can also be estimated from the width of the Bragg peak, Δq, using the Scherrer equation where $L = 2\pi K/\Delta q$ and the Scherrer constant, K, is taken as 0.94 (Smilgies, 2009). Taking into account the influence of instrumental broadening, Δq for the first Bragg peak is 0.0046 Å^{-1}; this gives a size of 1280 Å. This value is comparable

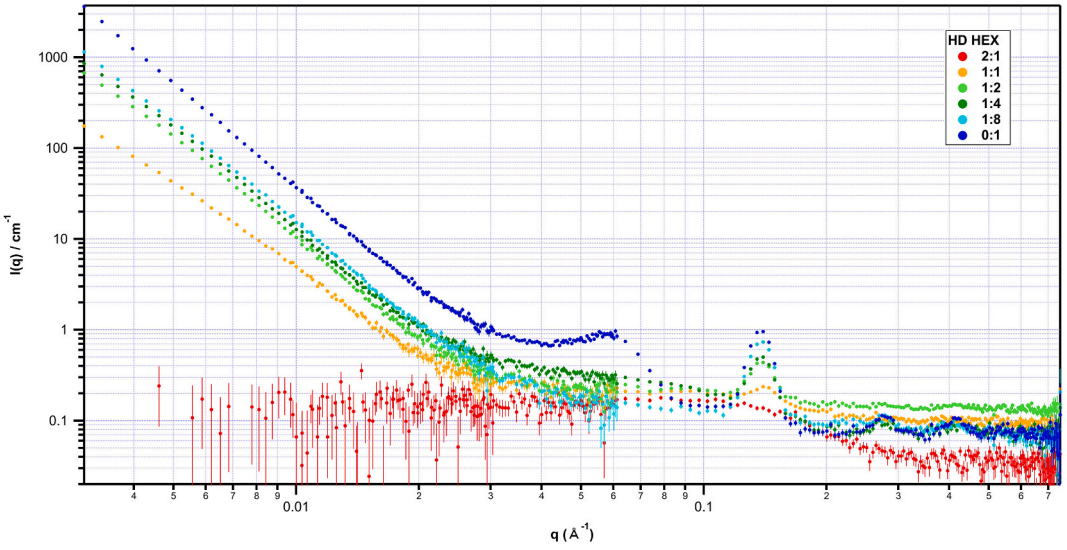

Fig. 6. SANS from 16 wt% samples prepared with hydrogenated hexadecane (i.e. HD contrast).

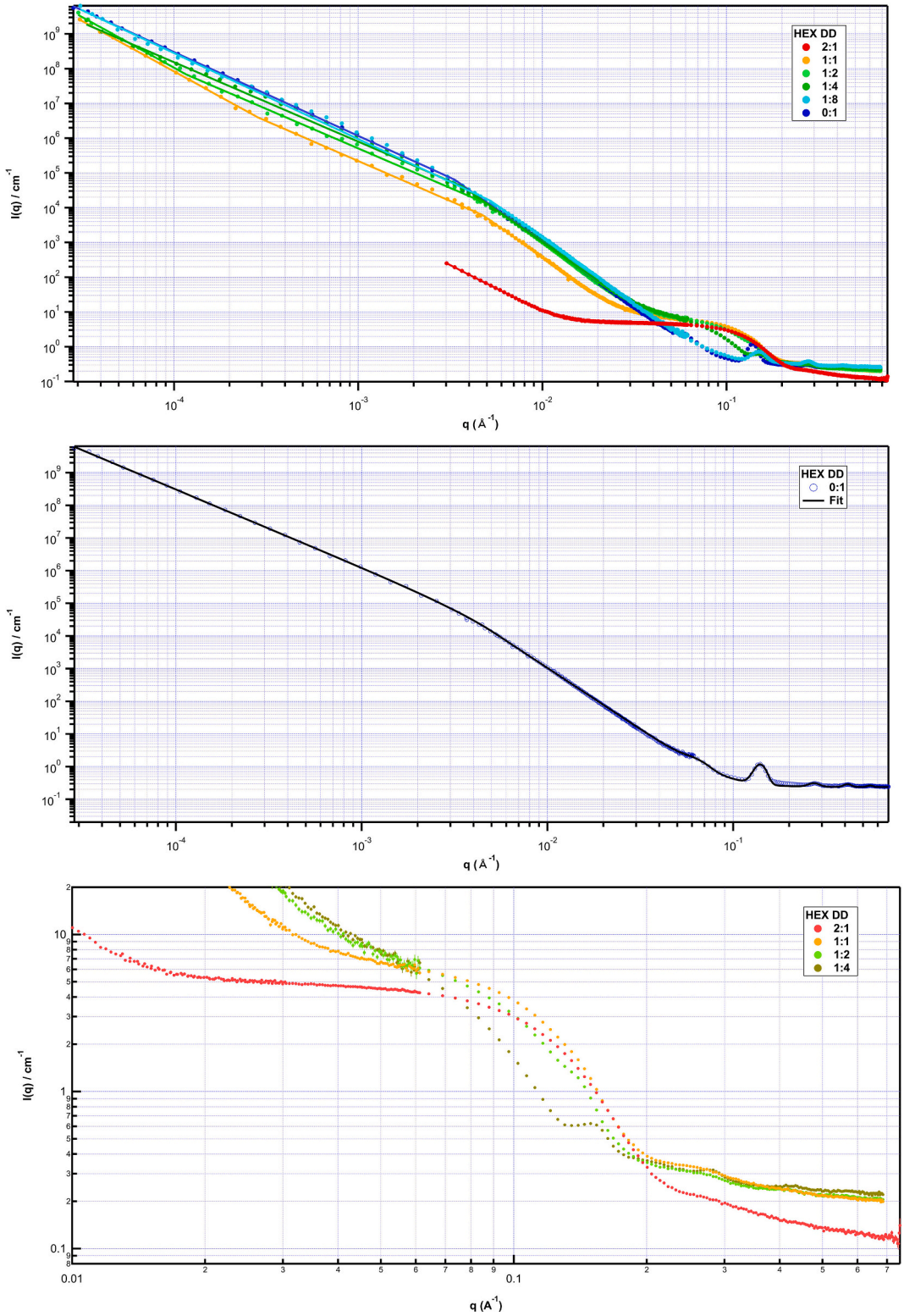

Fig. 7. (a) Combined USANS and SANS from 16 wt% samples prepared with deuterated hexadecane (i.e. DD contrast) including fits to single, double or triple power law as appropriate; (b) 0:1 data with fit to Guinier-Porod model plus five Gaussian peak function; (c) high q region showing micelle scattering for 2:1, 1:1, 1:2 and 1:4 samples.

to that obtained from the crossover value in q and provides an indication of the typical lateral dimension of an SO crystal that is responsible for the gel behaviour. The peak widths are essentially identical between the hexadecane and the TAG gels; however, unlike the low q intensity which was one order of magnitude greater compared to TAG, the Bragg peak intensity in the 0:1 hexadecane sample is approximately double that observed in the corresponding TAG samples. This indicates that at higher q, i.e. on the size range of the individual structurant molecules, the principal contrast arises from the difference between the hydrophilic and hydrophobic regions of the structurant, particularly any water

Table 4
Power law prefactor, exponents and crossover values for q from fits to USANS – SANS region using either one, two or three power law model, as appropriate, for DD samples. The standard deviation in the last digit of the fitting parameter is shown in parentheses.

OA: SO	Prefactor	Exponent 1	q_{c1} / Å^{-1}	Exponent 2	q_{c2} / Å^{-1}	Exponent 3
2:1	3.9(3) x 10^{-5}	–	–	–	–	2.70(2)
1:1	2.0(1) x 10^{-4}	2.905(6)	2.85 (9) x10^{-4}	2.302(6)	4.72(2) x10^{-3}	3.746(3)
1:2	2.2(2) x 10^{-4}	2.921(8)	1.16 (2) x10^{-4}	2.277(4)	5.07(2) x10^{-3}	3.795(4)
1:4	1.12(2) x 10^{-1}	–	–	2.284(2)	3.71(3) x10^{-3}	3.687(4)
1:8	3.66(5) x 10^{-2}	–	–	2.471(1)	5.23(3) x10^{-3}	3.762(4)
0:1	6.9(1) x $10^{-2.}$	–	–	2.410(2)	3.35(2) X10^{-3}	3.750(3)

associated with charged structurant headgroups.

The power-law slopes as a function of composition are shown in Table 4. The OA-containing samples exhibit broadly similar USANS in terms of the q value for the crossover region and a slightly higher Porod exponent but, in addition, exhibit a further crossover region at a lower q of ≈ 3–6 × 10^{-4} Å^{-1} where the power-law slope changes from ≈ 2.4 and ≈ 2.9 (in the limit of the USANS region); the latter exponent may suggest a transition towards denser mass fractal packing on the micron length scale. The different structures that give rise to these distinct scattering features will now be discussed in more detail.

3.7. Micellar structures

Multiple contrast (HD, DH and DD) data enable information on the component spatial distribution to be revealed and are shown for 2:1 in Fig. 8 and for 1:1 and 1:2 in Fig. S 3 in the Supplementary Material. All three 2:1 contrasts show scattering consistent with an inverse micellar structure, as previously reported for decane-based organogels (Nikiforidis et al., 2015). Guinier analysis yields radii of gyration, R_g which represent the root mean square distance of all scattering material from the centre of mass weighted by the scattering length density and is a simple but useful measure of the overall shape of the particle. R_g values obtained in this way give 7.5(9), 11.9(1) and 12.5(2) Å for the HD, DH and DD contrasts respectively. Notably, the HD sample (i.e. contrast between D_2O and all other hydrogenated components) suggests smaller scattering particles than DH and DD and gives some degree of information on the water located in the inverse micellar core. Assuming spherical geometry, the HD contrast can be used to estimate the core radius viz. $R_{core} = \sqrt{(5/3)}R_{g,HD} = 9.7$ Å. The DH contrast can equally well be used to estimate the spatial extent of the inverse micelle i.e. fully hydrogenated inverse micelle surrounded by deuterated solvent which yields a comparable dimension of $\sqrt{(5/3)}R_{g,DH} = 16.1$ Å.

While the Guinier analysis provides useful estimates, and requires no assumptions as to a model, it only uses a small fraction of the overall scattering data. To extract model dependent information, data for the

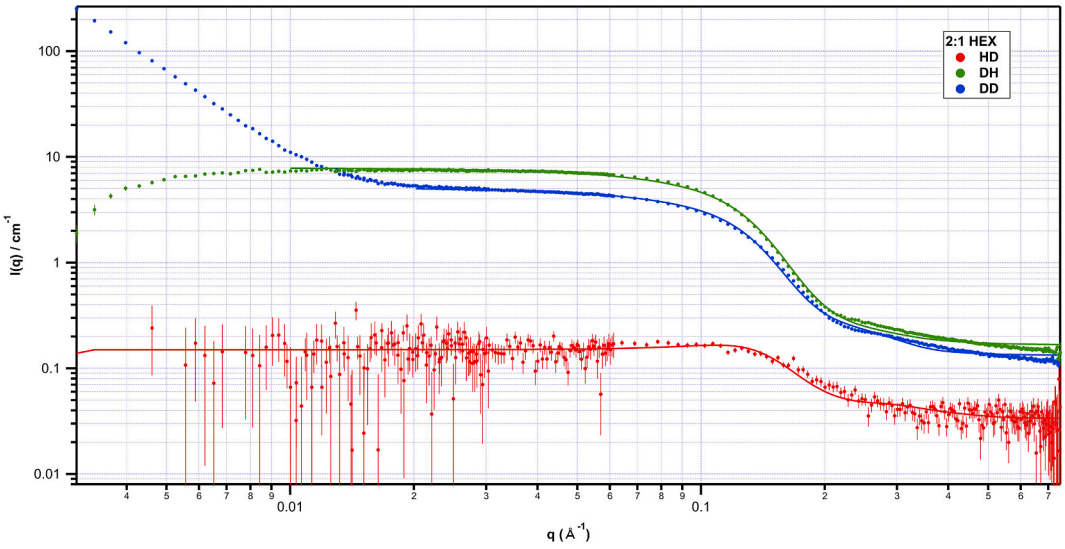

Fig. 8. Multiple contrast SANS from 2:1 organogels at 16 wt% structurant prepared in hexadecane. Lines show fits following simultaneous refinement using a model for polydisperse core-shell particles interacting with a hard sphere structure factor.

Table 5
Fit parameters to SANS data for 2:1 composition based on a polydisperse core-shell hard sphere interaction model (in which the core and shell have a fixed ratio) for the inverse micelles. The standard deviation in the last digit of the fitting parameter is shown in parentheses.

	HD	DH	DD
volume fraction	0.203(4)	0.176(1)	0.156(1)
avg core rad (Å)		6.01(3)	
Shell thickness (Å)		13.02(3)	
Core polydispersity		0.2695(8)	
SLD core (Å^{-2})	6.34 × 10^{-6} (fixed)	−0.56 × 10^{-6} (fixed)	6.34 × 10^{-6} (fixed)
SLD shell (Å^{-2})	0.035(7) x 10^{-6}	1.57(1) x 10^{-6}	2.366(9) x 10^{-6}
SLD solvent (Å^{-2})	−0.440 × 10^{-6} (fixed)	6.74 × 10^{-6} (fixed)	6.74 × 10^{-6} (fixed)
Background (cm^{-1})	0.0334(6)	0.1668(2)	0.1322(2)

three contrasts were simultaneously fitted to a polydisperse core-shell hard sphere interaction model (in which the core and shell have a fixed ratio) while constraining the neutron scattering length densities of the core and solvent (based on values in Tables 1). The drop in intensity for the DH sample arises from background subtraction of the deuterated oil which itself contains dissolved air bubbles that generate a finite upturn in scattering at low q; along with the low q upturn in the DD sample, both regions have been excluded in the fits. The resultant fits are shown in Fig. 8 and associated parameters in Table 5. The values obtained for volume fraction (16–20%) are in good agreement with the known concentration of components in the formulations. The core and shell dimensions are 6 and 13 Å respectively.

Based on the reported crystal structures of OA and SO, the length of a fully extended structurant molecule, R_{chain}, is approximately 20–23 Å. Therefore, the shell of the inverse micelle might be expected to take similar values. The smaller radius obtained is a consequence of the apolar solvent being a good solvent for the structurant chains and the solvent penetrating into the shell. The SLD for the 2:1 structurant composition can be calculated to be 0.120×10^{-6}. This is close to the refined value for the HD contrast but for the DH and DD contrasts, larger fitted values are returned. Indeed, the latter is consistent with solvation of the structurant shell by the surrounding (deuterated) solvent. Notably the 2:1 DD sample exhibited an upturn at low q which was not observed for the other contrasts and indicates the presence of some large-scale structure formation i.e. crystalline material; the latter may be partly due to the formulations having been prepared on a weight basis (the HD sample corresponds to a structurant volume fraction of 14.1% whereas the DH and DD samples correspond to 15.8%).

A comparison of the 2:1 SANS with HD contrast at decreasing structurant concentration (i.e. 16 to 8 to 4 wt%, data not shown) reveals that the inverse micelle core dimensions increase, reaching an $R_g \approx 12.8$ Å for 4 wt%. A structurant concentration of 16 wt% corresponds approximately to an equimolar ratio of structurant to water. Since water and hexadecane are immiscible, the same amount of water must be accommodated by less structurant as the structurant concentration decreases from 16 to 4 wt%. This would inevitably lead to inverse micelles with larger aqueous cores. No Bragg peaks are present in any of the 2:1 samples although, again, it is possible that the micelle scattering masks weak Bragg peaks as is observed for the 1:1, 1:2 compositions at 16 wt% which exhibit coexistence of micellar and crystalline lamellar structures (Fig. S3). The dimensions of the micellar structures for 1:1 and 1:2 are similar to 2:1 (Fig. 7 b), but smaller than those at 1:4. However, the lack of a defined Guinier region in the scattering patterns precludes a detailed evaluation of their dimensions.

3.8. SO structuring

The pure SO organogels, i.e. structurant ratio 0:1, exhibit the simplest scattering patterns. The HD, DD and DH contrast SANS data for 0:1 16 wt% are shown in Fig. 9. All three patterns comprise power law scattering and a series of Bragg peaks with a $q \approx 0.14$ Å^{-1} parent structure. Crystalline SO must be responsible for this series of Bragg peaks as the system does not contain OA. The observed scattering is reminiscent of the formation of crystalline nanoplatelets from TAGs (Ramel, Co, Acevedo, & Marangoni, 2016) and whose dimensions are of the order of 1280 Å as calculated above. As explained previously, the low q scattering intensities are approximately the same for DD as DH and predictably more than one order of magnitude greater than HD; this immediately demonstrates that the dominant contrast giving rise to large-scale structure formation is between the structurant (hydrogenated) molecules and the (deuterated, in both DD and DH) oil. However, DH and HD share an additional feature at $q \approx 0.055$ Å^{-1}, which DD does not exhibit. This indicates that the low q scattering and the 0.055 Å^{-1} feature cannot share a common origin. In addition, the intensity of Bragg peaks for HD and DD are comparable and greater than DH as expected based on the principal contrast arising in this q range from the difference between the hydrophilic and hydrophobic regions of the structurant. It is noted that the higher order Bragg reflections are more observable in HD, primarily due to an apparent lower level of background scattering. Given that the low q scattering is similar for DD and DH and Bragg peak scattering is similar for DD and HD but there is a lack of the 0.055 Å^{-1} peak only for DD, its absence is thus unrelated to the contrast and may merely indicate that the structurant has remained predominantly as crystalline lamellae and simply not formed this additional structure. Having said this, its origin does appear to be chain-length dependent since it is not observed in formulations using decane instead of hexadecane (Fig. S 4 in Supplementary Material). This effect may be due to chain length similarity between hexadecane and oleate or the solvent having a melting point closer to room temperature (18 °C compared to −30 °C for decane) enabling a greater propensity for structuring.

It is of interest to evaluate changes in the scattering from the ≈ 0.055 Å^{-1} peak as a function of structurant concentration. The SANS for the 0:1 samples prepared at 4, 8 and 16 wt% structurant is shown in Fig. 10 a; also shown for comparison is SAXS data for the same samples that have been normalised at high q (Fig. 10 b). It is evident, particularly in the SAXS, that the Bragg peaks and the power law scattering at low q are

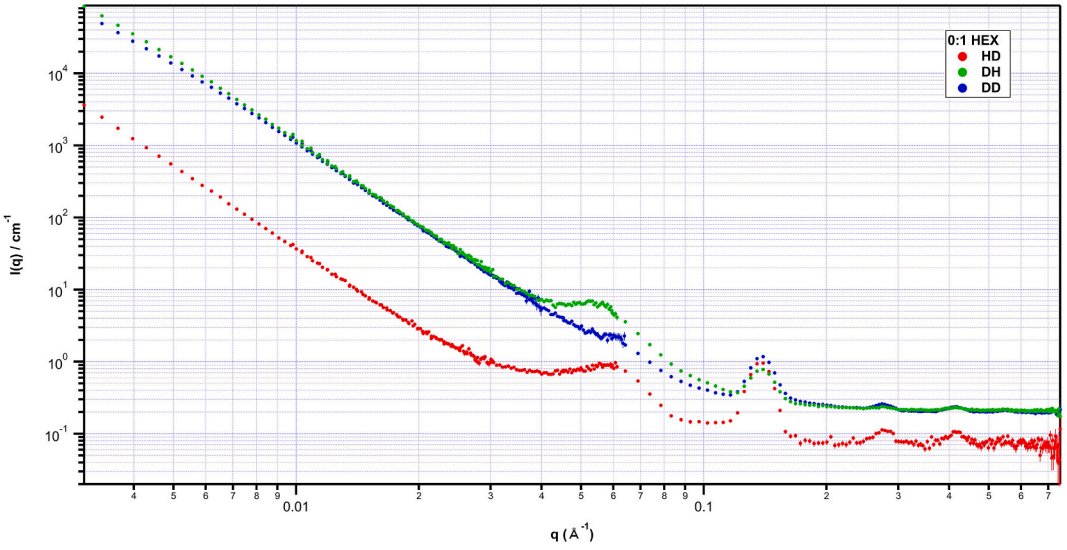

Fig. 9. Multiple contrast SANS from 0:1 organogels at 16 wt% structurant prepared in hexadecane.

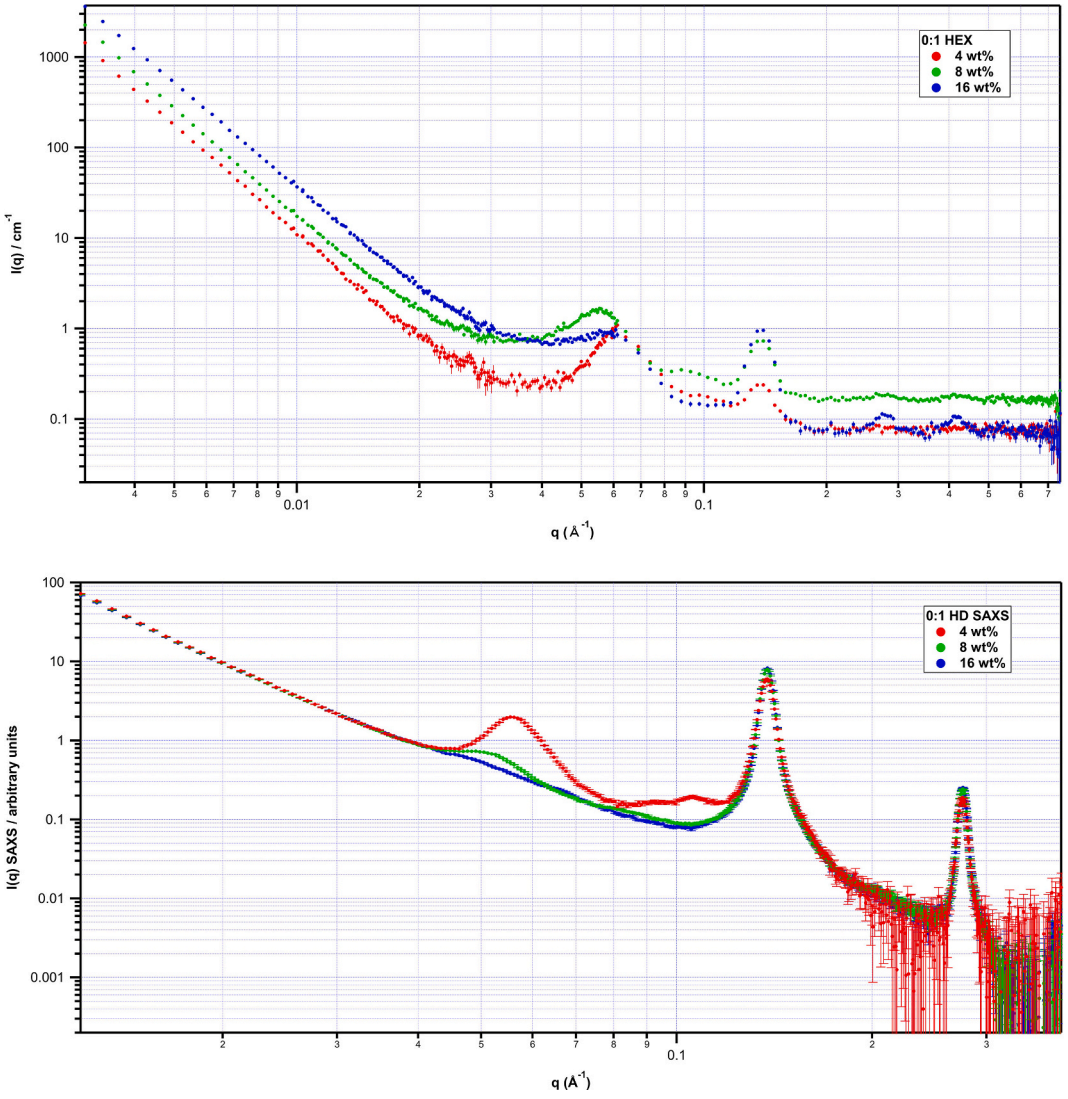

Fig. 10. (a) SANS and (b) SAXS from 4, 8 and 16 wt% 0:1 HD contrast samples prepared with hydrogenated hexadecane.

perfectly correlated and therefore must be associated with the same structure. In addition, these features are completely independent of the scattering feature at ≈ 0.055 $Å^{-1}$. The latter feature appears to shift to higher q (shorter d-spacing) as the structurant concentration decreases i.e. with increasing number of water molecules per structurant molecule. At 4 wt%, a second order reflection is present. Again, since these samples have 0:1 composition, the effect can only be due to changes in SO concentration. While the origin of the peak is unclear, it is likely to be associated with the arrangement of water within structures with a separation of ≈ 100 Å which may be tentatively attributed to a minor co-existing, possibly thermodynamically unstable lamellar liquid crystalline structure (Borné, Nylander, & Khan, 2001; Edwards, Silvander, & Karlsson, 1995; Mele et al., 2018; Rong & Qing-Hong, 2000; Seddon, Bartle, & Mingins, 1990).

4. General discussion

The results obtained have shown that the gel strength of OA-SO oleogels is primarily due to SO. Gel formation was associated with an increase in the presence of large-scale structures that have the ability to generate space-filling networks. However, OA was demonstrated to play a role as it has a profound negative effect on gel strength and large-scale structure formation. SANS experiments on gels formed in TAGs and the solvent analogue C_{16} (hexadecane) indicated that, as the ratio between OA and SO was varied, structures are present, comprising inverse micelles, crystals forming a space-filling network composed of lamellae and, in hexadecane, additional lamellar liquid crystals. The geometry of the structures formed, and their relative proportions, may be explained simplistically on the basis of the critical packing parameter, or cpp (Israelachvili, Mitchell, & Ninham, 1976). The cpp is given as $cpp = v_o/al_o$, where v_o and l_o are the volume and the length of the average structurant molecule and a is the surface area of the structurant tail (which is the same for OA and SO). For 16 wt% 2:1, the system is dominated by hydrophobic interactions between the OA tails and the oil. The OA headgroup is small compared to the oleic tail and $v_o/al_o > 1$. The 1 wt% water is located around the acidic headgroups and the formation of inverse spherical micelles is favoured (Nikiforidis et al., 2015). Such micellar structures are incapable of forming a space-filling network. Therefore, any 'solid-like' properties in these OA-rich systems must arise from the presence of large-scale structures, which are associated with SO. Even then, 2:1 gels have a significantly lower G* than samples containing greater amounts of SO. The presence of sodium in the SO headgroup provides SO with greater polarity, hydrophilicity, and results in a reduction in the cpp. Hence, with increasing addition of SO, the average cpp of the structurant is reduced and structures with reduced curvature are favoured leading to the formation of lamellar liquid

crystals. This is apparent, for example, in the 0.055 $Å^{-1}$ and 0.105 $Å^{-1}$ peaks observed in the 0:1 4 wt% samples. There is no evidence in the scattering for any other potential structures (e.g. inverse discontinuous, inverse hexagonal or inverse bi-continuous phases (Seddon et al., 1990)) in any of the SANS patterns obtained.

The phase diagram presented by Tandon et al. (Fig. 1) for mixtures of OA and SO provided a rationale for many of our observations. Pure SO (0:1), is expected to be insoluble in apolar solvents such as TAG oils and C_{16}. Hence, the 0:1 samples are likely to principally be dispersions of SO crystals while an additional liquid crystalline phase may be formed at lower structurant concentrations. As OA is added to the formulation, SO is partially dissolved at elevated temperatures. Consequently, a proportion of the SO can be incorporated into mixed crystals or, although less likely, an equimolar complex with OA, upon heating during the gel preparation. The incorporation of OA results is a reduction in the gel strength. This finding differs from an earlier study (Nikiforidis et al., 2015) for samples prepared with decane, as opposed to hexadecane here, where a maximum in storage modulus was found for a 1:1 ratio. This was proposed to represent a synergistic effect between OA and SO and attributed to the formation of a complex responsible for generating the gel-forming network. However, it is noted that the previous SANS data, which were collected for fewer compositions, demonstrated the same positive relationship between SO content and low q intensity as found here; in addition, the SANS data collected showed no signatures of any crystal structure except for the pure SO system. The poorer purity of components utilised may explain the discrepancy. In the OA-rich side of the phase diagram, OA can dissolve some SO at room temperature. This SO may be partially incorporated in the inverse micellar structures found in the OA-rich samples (i.e. 2:1, 1:1) with the effect of decreasing the extent of large-scale structure formation. This can also explain the accompanied reduction in low-q scattering, and the consequent observed reduction in gel strength. The crystals observed in the 2:1 samples via microscopy, and the presence of an upturn in SANS intensity at low q, nonetheless indicate that, even for low concentrations of SO, micelles and crystals can co-exist. The tunability in behaviour has some similarities to the lecithin-stearic acid oleogel systems where increasing stearic acid leads to enhanced gel strength (Gaudino, Ghazani, Clark, Marangoni, & Acevedo, 2019). We also note that the subject of tunability in oleogel behaviour has been recently discussed in phytosterol/monoglyceride (Yang, Chen, & Yang, 2018) and glyceryl/sorbitan tristearate/monostearate oleogels (Cerqueira et al., 2017).

While the arsenal of techniques employed here provide a detailed understanding into these oleogels, it would be valuable to conduct a thorough complementary examination of all compositions using thermal techniques. This would enable a direct comparison to be made between the pure structurant system(s), i.e. combinations of OA and SO, and those in the gel systems that additionally contain oil and water. It is also noted that the extent to which deuteration may independently affect gel strength or microscopic structure would also be valuable.

5. Conclusions

The formation of OA-SO oleogels has been studied using a combination of techniques, including rheology, microscopy, small-angle neutron scattering and ultra-small angle neutron scattering. Together, these techniques provide insight into the relation between structure on the micro- and nanoscale and bulk (macroscale) mechanical behaviour. SO is demonstrated to play a critical role as the principal oleogelator and imparts solid-like behaviour to the oil. However, the presence of OA enables the overall gel properties to be finely tuned. Indeed, varying the ratio between SO and OA can provide control over the melting behaviour of the oleogel, as well as the mechanical properties. The concept of combining two gelators with opposing functionality may provide inspiration for future studies on the creation of oleogels with tunable properties. Such control is important when considering future applications.

It is important to note that, from a food perspective, the high amounts of OA or SO studied here would be unsuitable for a food product as, for example, free fatty acids are deleterious to health at concentrations above approximately 3%; however, the methodology presented here should assist in the predictive design of oleogel systems with direct food application. In addition, while solvent contrast variation SANS and USANS have been employed to provide detail on the structures formed in these gel systems, the conclusions drawn from the use of apolar solvents, such as hexadecane, must be moderated as far as a comprehensive understanding of the TAG systems is concerned due to differences in solvent polarity between hexadecane and the TAG oils. Nonetheless, the similarity in structures formed is notable and demonstrates the value of this approach. The availability of deuterated edible oils via solvent contrast variation, as well as deuterated structurants, would provide the opportunity for further, more elaborate, SANS studies to be pursued for food-relevant systems; the syntheses of the latter are currently the subject of active investigation.

Declaration of Competing Interest

none.

Acknowledgements

We would like to thank Anna Sokolova and Andrew Whitten for their assistance with the preliminary SANS measurements performed on the BILBY instrument and Robert Knott for assistance with SAXS measurements. This work benefited from the use of the SasView application, originally developed under NSF award DMR-0520547. SasView contains code developed with funding from the European Union's Horizon 2020 research and innovation programme under the SINE2020 project, grant agreement No 654000.

Appendix A. Supplementary data

Supplementary data to this article can be found online at https://doi.org/10.1016/j.ifset.2021.102763.

References

Babu, S. S., Prasanthkumar, S., & Ajayaghosh, A. (2012). Self-assembled gelators for organic electronics. *Angewandte Chemie - International Edition, 51*(8), 1766–1776. https://doi.org/10.1002/anie.201106767

Bhatia, A., Singh, B., Raza, K., Wadhwa, S., & Katare, O. P. (2013). Tamoxifen-loaded lecithin organogel (LO) for topical application: Development, optimization and characterization. *International Journal of Pharmaceutics, 444*(1–2), 47–59. https://doi.org/10.1016/j.ijpharm.2013.01.029

Borné, J., Nylander, T., & Khan, A. (2001). Phase behavior and aggregate formation for the aqueous monoolein system mixed with sodium oleate and oleic acid. *Langmuir, 17*(25), 7742–7751. https://doi.org/10.1021/la010650w

Bot, A., Gilbert, E. P., Bouwman, W. G., Sawalha, H., den Adel, R., Garamus, V. M., … Flöter, E. (2012). Elucidation of density profile of self-assembled sitosterol + oryzanol tubules with small-angle neutron scattering. *Faraday Discussions, 158*, 223. https://doi.org/10.1039/c2fd20020a

Cerqueira, M. A., Fasolin, L. H., Picone, C. S. F., Pastrana, L. M., Cunha, R. L., & Vicente, A. A. (2017). Structural and mechanical properties of organogels: Role of oil and gelator molecular structure. *Food Research International, 96*, 161–170. https://doi.org/10.1016/j.foodres.2017.03.021

Curat, J. L., & Perron, R. (1977). Polymorphisme de l'oleate de sodium anhydre. *Chemistry and Physics of Lipids, 19*, 301–311.

Davidovich-Pinhas, M., Barbut, S., & Marangoni, A. G. (2016). Development, characterization, and utilization of food-grade polymer Oleogels. *Annual Review of Food Science and Technology, 7*(January), 65–91. https://doi.org/10.1146/annurev-food-041715-033225

Edwards, K., Silvander, M., & Karlsson, G. (1995). Aggregate structure in dilute aqueous dispersions of oleic acid/sodium Oleate and oleic acid/sodium Oleate/egg phosphatidylcholine. *Langmuir, 11*(7), 2429–2434. https://doi.org/10.1021/la00007a020

Gao, Z. F., Liu, R., Wang, J., Dai, J., Huang, W. H., Liu, M., … Jiang, L. (2018). Controlling droplet motion on an Organogel surface by tuning the chain length of DNA and its biosensing application. *Chem, 4*(12), 2929–2943. https://doi.org/10.1016/j.chempr.2018.09.028

Gaudino, N., Ghazani, S. M., Clark, S., Marangoni, A. G., & Acevedo, N. C. (2019). Development of lecithin and stearic acid based oleogels and oleogel emulsions for

edible semisolid applications. *Food Research International, 116*(September 2018), 79–89. https://doi.org/10.1016/j.foodres.2018.12.021

Gilbert, E. P. (2019). Small-angle X-ray and neutron scattering in food colloids. *Current Opinion in Colloid and Interface Science, 42*, 55–72. https://doi.org/10.1016/j.cocis.2019.03.005

Gilbert, E. P., Schulz, J. C., & Noakes, J. T. (2006). "Quokka" - the small-angle neutron scattering instrument at OPAL. *Physica B*, 385–386.

Gravelle, A. J., Davidovich-Pinhas, M., Zetzl, A. K., Barbut, S., & Marangoni, A. G. (2015). Influence of solvent quality on the mechanical strength of ethylcellulose oleogels. *Carbohydrate Polymers, submitted*, 169–179. https://doi.org/10.1016/j.carbpol.2015.08.050

Hughes, N. E., Marangoni, A. G., Wright, A. J., Rogers, M.a., & Rush, J. W. E. E. (2009). Potential food applications of edible oil organogels. *Trends in Food Science & Technology, 20*(10), 470–480. https://doi.org/10.1016/j.tifs.2009.06.002

Israelachvili, J. N., Mitchell, D. J., & Ninham, B. W. (1976). Theory of self-assembly of hydrocarbon amphiphiles into micelles and bilayers. *Journal of the Chemical Society, Faraday Transactions, 2*(72), 1525. https://doi.org/10.1039/f29767201525

Jandacek, R. J., & Broering, W. B. (1989). X-ray diffraction study of sodium soaps of monounsaturated and polyunsaturated fatty acids. *Lipids, 24*(12), 1008–1013. https://doi.org/10.1007/BF02544070

Kaneko, F., Yamazaki, K., Kitagawa, K., & Kikyo, T. (1997). Structure and crystallization behavior of the phase of oleic acid. *Journal of Physical Chemistry B, 5647*(96), 1803–1809. https://doi.org/10.1021/jp963400a

Kline, S. R. (2006). Reduction and analysis of SANS and USANS data using IGOR pro. *Journal of Applied Crystallography, 39*(6), 895–900. https://doi.org/10.1107/S0021889806035059

Kostik, V., Memeti, S., & Bauer, B. (2012). Fatty acid composition of edible oils and fats. *Journal of hygienic engineering and …, 3–7, 4*, 112–116. Retrieved fromhttp://www.jhed.mk/filemanager/JHED Vol 4/02. FPP/06. Full paper - Vesna Kostik 2.Pdf.

Kubo, W., Murakoshi, K., Kitamura, T., Yoshida, S., Haruki, M., Hanabusa, K., … Yanagida, S. (2001). Quasi-solid-state dye-sensitized TiO2 solar cells: Effective charge transport in mesoporous space filled with gel electrolytes containing iodide and iodine. *Journal of Physical Chemistry B, 105*(51), 12809–12815. https://doi.org/10.1021/jp012026y

Martins, A. J., Cerqueira, M. A., Fasolin, L. H., Cunha, R. L., & Vicente, A. A. (2016). Beeswax organogels: Influence of gelator concentration and oil type in the gelation process. *Food Research International, 84*, 170–179. https://doi.org/10.1016/j.foodres.2016.03.035

Mele, S., Söderman, O., Ljusberg-Wahrén, H., Thuresson, K., Monduzzi, M., & Nylander, T. (2018). Phase behavior in the biologically important oleic acid/sodium oleate/water system. *Chemistry and Physics of Lipids, 211*(September 2017), 30–36. https://doi.org/10.1016/j.chemphyslip.2017.11.017

Nikiforidis, C. V., Gilbert, E. P., & Scholten, E. (2015). Organogel formation via supramolecular assembly of oleic acid and sodium oleate. *RSC Advances, 5*(59), 47466–47475. https://doi.org/10.1039/c5ra05336f

Nikiforidis, C. V., & Scholten, E. (2014). Self-assemblies of lecithin and α-tocopherol as gelators of lipid material. *RSC Advances, 4*(5), 2466–2473. https://doi.org/10.1039/C3RA46584E

Ramel, P. R., Co, E. D., Acevedo, N. C., & Marangoni, A. G. (2016). Structure and functionality of nanostructured triacylglycerol crystal networks. *Progress in Lipid Research, 64*, 231–242. https://doi.org/10.1016/j.plipres.2016.09.004

Raynal, M., & Bouteiller, L. (2011). Organogel formation rationalized by Hansen solubility parameters. *Chemical Communications, 47*(29), 8271. https://doi.org/10.1039/c1cc13244j

Rehm, C., Brûlé, A., Freund, A. K., & Kennedy, S. J. (2013). Kookaburra: The ultra-small-angle neutron scattering instrument at OPAL. *Journal of Applied Crystallography, 46* (2011), 1699–1704. https://doi.org/10.1107/S0021889813025788

Rehm, C., De Campo, L., Brûlé, A., Darmann, F., Bartsch, F., & Berry, A. (2018). Design and performance of the variable-wavelength, Bonse-Hart ultra-small-angle neutron scattering diffractometer KOOKABURRA at ANSTO. *Journal of Applied Crystallography, 51*(1), 1–8. https://doi.org/10.1107/S1600576717016879

Rogers, M. A. (2018). Hansen solubility parameters as a tool in the quest for new edible Oleogels. *JAOCS, Journal of the American Oil Chemists' Society, 95*(4), 393–405. https://doi.org/10.1002/aocs.12050

Rogers, M. A., Strober, T., Bot, A., Toro-Vazquez, J. F., Stortz, T., & Marangoni, A. G. (2014). Edible oleogels in molecular gastronomy. *International Journal of Gastronomy and Food Science, 2*(1), 1–10. https://doi.org/10.1016/j.ijgfs.2014.05.001

Rong, G., & Qing-Hong, F. (2000). Lamellar liquid crystal polymerization of sodium oleate/oleic acid/octadiene/water system. *Chinese Journal of Chemistry, 18*(1). https://doi.org/10.1002/cjoc.20000180103/abstract. Retrieved from.

Rosen-Kligvasser, J., & Davidovich-Pinhas, M. (2021). The role of hydrogen bonds in TAG derivative-based oleogel structure and properties. *Food Chemistry, 334*(May 2020), 127585. https://doi.org/10.1016/j.foodchem.2020.127585

Ru, Y., Fang, R., Gu, Z., Jiang, L., & Liu, M. (2020). Reversibly Thermosecreting Organogels with switchable lubrication and anti-icing performance. *Angewandte Chemie - International Edition, 59*(29), 11876–11880. https://doi.org/10.1002/anie.202004122

Sawalha, H., Venema, P., Bot, A., Flöter, E., Lan, Y., & van der Linden, E. (2020). Effects of oil type on sterol-based Organogels and emulsions. *Food Biophysics*, 109–118. https://doi.org/10.1007/s11483-020-09654-8

Seddon, J. M., Bartle, E. A., & Mingins, J. (1990). Inverse cubic liquid-crystalline phases of phospholipids and related lyotropic systems. *Journal of Physics: Condensed Matter*, 2. https://doi.org/10.1088/0953-8984/2/S/043

Smilgies, D. M. (2009). Scherrer grain-size analysis adapted to grazing-incidence scattering with area detectors. *Journal of Applied Crystallography, 42*(6), 1030–1034. https://doi.org/10.1107/S0021889809040126

Tandon, P., Förster, G., Neubert, R., & Wartewig, S. (2000). Phase transitions in oleic acid as studied by X-ray diffraction and FT-Raman spectroscopy. *Journal of Molecular Structure, 524*(1–3), 201–215. https://doi.org/10.1016/S0022-2860(00)00378-1

Tandon, P., Neubert, R., & Wartewig, S. (2000). Thermotropic phase behaviour of sodium oleate as studied by FT-Raman spectroscopy and X-ray diffraction. *Journal of Molecular Structure, 526*(1–3), 49–57. https://doi.org/10.1016/S0022-2860(00)00441-5

Tandon, P., Raudenkolb, S., Neubert, R. H. H., Rettig, W., & Wartewig, S. (2001a). X-ray diffraction and spectroscopic studies of oleic acid-sodium oleate. *Chemistry and Physics of Lipids, 109*(1), 37–45. https://doi.org/10.1016/S0009-3084(00)00207-3

Tandon, P., Raudenkolb, S., Neubert, R. H. H., Rettig, W., & Wartewig, S. (2001b). X-ray diffraction and spectroscopic studies of oleic acid-sodium oleate. *Chemistry and Physics of Lipids, 109*(1), 37–45. https://doi.org/10.1016/S0009-3084(00)00207-3

Unger, M., Chaturvedi, D., Mishra, S., Tandon, P., & Siesler, H. W. (2013). Two-dimensional correlation analysis of temperature-dependent FT-IR spectra of oleic acid. *Spectroscopy Letters, 46*(1), 21–27. https://doi.org/10.1080/00387010.2012.659368

Wood, K., Mata, J. P., Garvey, C. J., Wu, C. M., Hamilton, W. A., Abbeywick, P., … Gilbert, E. P. (2018). QUOKKA, the pinhole small-angle neutron scattering instrument at the OPAL research reactor, Australia: Design, performance, operation and scientific highlights. *Journal of Applied Crystallography, 51*(2), 294–314. https://doi.org/10.1107/S1600576718002534

Yang, D. X., Chen, X. W., & Yang, X. Q. (2018). Phytosterol-based oleogels self-assembled with monoglyceride for controlled volatile release. *Journal of the Science of Food and Agriculture, 98*(2), 582–589. https://doi.org/10.1002/jsfa.8500